Asian Journal of Chemistry; Vol. 36, No. 7 (2024), 1579-1586

ASIAN JOURNAL OF CHEMISTRY

https://doi.org/10.14233/ajchem.2024.31471

Effect of Zinc Doping and Porosity on Structural, Morphological and Gas Sensing Properties of Porous Zn:SnO_2 Bilayer Thin Film

R. YOGASARASWATHI* and J. DHEEPA

PG and Research Department in Physics, Government Arts College (Autonomous), Coimbatore-641018, India

*Corresponding author: E-mail: yogasaraswathi.astro@gmail.com

Received: 4 March 2024; *Accepted*: 10 May 2024; *Published online*: 29 June 2024; AJC-21677

The automated nebulizer spray pyrolysis technique was used to synthesize porous SnO_2 bilayer thin films as well as doped porous SnO_2 bilayer thin films with varying zinc doping percentages. The synthesized thin films were characterized using X-ray diffraction, field emission scanning electron microscopy, energy dispersive analysis of X-rays, UV-Vis spectroscopy, photoluminescence spectroscopy, current-voltage characteristics and gas sensing performance. The effect of doping on sensor response was investigated using various gases and operating temperatures. The optimized Zn-doped porous SnO_2/SnO_2 gas sensor sample was taken to further gas sensing analysis. The results revealed that the doping of zinc with a porous tin oxide bilayer increases the gas sensor response at low operating temperatures compared to undoped porous tin oxide bilayers and it also reduces the response recovery time of the sensor. The response of the sensor in a CO gas concentration of 400 ppm has been improved with good repeatability.

Keywords: Porous SnO_2, Bilayer films, Zinc doping, Automated nebulizer spray technique, CO gas sensor.

INTRODUCTION

Several studies have been carried out to develop effective gas sensors that can detect trace levels of pollution from a variety of sources because of the awareness of the health risks associated with various dangerous and polluting gases and the need to resolve these risks by executing stronger regulations [1-4]. To sense different harmful gases, thin film, ultrathin film and nanostructure materials made of polymers, metal oxide semiconductors, metal, carbon nanotube, graphene, *etc*. have been studied. To achieve high sensitivity, selectivity, quick reaction, *etc*., new device structures have been developed. It is found that the microstructure and film thickness have a significant impact on gas sensing performance [5-7].

Demonstrating the ability of nanostructured materials to sense different gases has become a standard procedure in the field of environment gas sensors. As civilization has advanced, environmental gas pollution has become a major problem for society [8-10]. This present work deals with the effect of doping and porosity on the microstructural and gas-sensing behaviour of porous Zn-doped SnO_2 bilayer thin films.

EXPERIMENTAL

Tin(II) chloride dihydrate ($SnCl_2{\cdot}2H_2O$, 99.99%) and zinc chloride ($ZnCl_2$, ≥ 98%) as dopant were procured from Merck Ltd., India. PEG-1500 (99%) and C_2H_5OH (99.9%) were of analytical grade chemicals and utilized without further purification. The automated nebulizer spray pyrolysis technique was used to deposit porous Zn:SnO_2/SnO_2 thin films on the clean glass substrates. Tin oxide based thin films were prepared from tin chloride dihydrate ($SnCl_2{\cdot}2H_2O$). A 3:1 ratio of ethanol and double-distilled water was combined to create a solvent solution. To achieve the desired precursor solution, an exactly measured amount of calculated tin chloride was mixed with the solvent solution. The tin chloride concentration was maintained at 0.3 M for pure SnO_2.

Preparation of porous Zn:SnO_2/SnO_2 film: The automated nebulizer spray pyrolysis technique was used to deposit porous Zn:SnO_2/SnO_2 thin films on the clean glass substrates. Tin oxide based thin films were prepared from tin chloride. To achieve the desired precursor solution, an exactly measured amount of calculated tin chloride was mixed with the solvent solution.

The tin chloride concentration was maintained at 0.3 M for pure SnO_2 base layer. Next, the mixture was stirred using a magnetic stirrer until a transparent precursor solution is achieved. Besides, the substrates were cleaned ultrasonically with distilled water and an acetone mixture for 5 min. Then the substrates were quickly dried with cotton balls before being placed on the hot plate that had been pre-heated already. Precursor solution was first transferred into the solution container and then sprayed onto the glass substrate, which was already heated to 450 ºC on a hot plate. The pressure of the carrier gas was maintained at 30 Pa. The distance between the spray nozzle and the substrate was 10 cm. A 0.1 mL/min was the constant spray rate used in the experiment and 5 mL was the coating volume for pure SnO_2. To coat an additional layer of porous zinc doped SnO_2 on a pure tin oxide surface, the optimized amount of 0.2 M tin chloride and PEG-1500 acted as the porogen [11-14] were added in a solvent solution and the mixture was stirred well for 5 min. Then zinc chloride was added as a dopant in the precursor solution with a doping percentage of 1, 2 and 3%. After achieving the lumpless white solution, it was transferred into the container and sprayed on a pure SnO_2 layer and the coating volume is 1mL for porous Zn:SnO_2 bilayer. After deposition, the films were allowed to cool at room temperature [15-17].

Characterization: A powder-XRD (XRD7000 diffractometer, USA) was used to obtain XRD difraction patterns of the prepared thin films with a scan rate of 0.03º/sec and the data were recorded in the range of 2θ = 10º to 70º on a Cu*K*α radiation beam operated at 30 kV and 25 mA at 25 ºC. A SEM (LEO 1450 VP instrument) was used to conduct elemental and compositional investigations on the thin-film samples, as well as field emission scanning electron microscopy (FESEM) to characterize their surface shape. The UV visible spectra of the thin films were measured using double beam UV–Vis spectrophotometer (Perkin-Elmer: Lambda35) over a wavelength range of 190-1100 nm. In order to carry out the photoluminescence spectra, a FluoroMax-3 and a 450W xenon arc source were utilized.

RESULTS AND DISCUSSION

X-ray diffraction (XRD) studies: Using an XRD pattern, the structural characteristics of the prepared thin films were examined within the range of diffraction angles from 15º to 60º. The diffraction peak in the pattern corresponds to a tetragonal rutile structure. The presence of the broad peaks in the XRD patterns (Fig. 1) indicates the polycrystalline nature and it shows preferential orientation along with the maximum intensity peak from (110). The results are matched with the reported

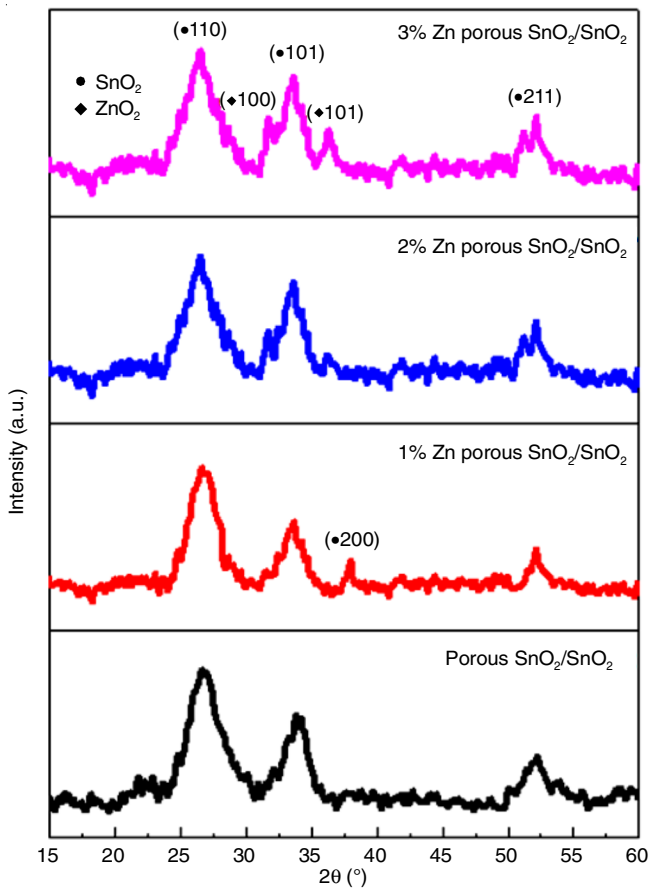

Fig. 1. XRD pattern of Zn:SnO_2 based bilayer thin films

JCPDS data (card no. 41-1445), from many SnO_2 thin film articles [18-20]. The peaks at 2θ = 26.61º, 33.89º and 51.78º correspond to the (110), (101) and (211) planes in porous Zn:SnO_2 bilayer films, respectively. With 1% of Zn doping has all the predominant peaks including (200) plane was established on 2θ = 37.95º with good intensity and there is no shift due to 1% of Zn doping.

The calculated grain size D is in the range of 33.72, 45.11, 49.02 and 51.33 nm for porous Zn:SnO_2 bilayer films at different doping percentages of 0, 1, 2 and 3%, respectively. Grain size increases with increasing the dopant percentage it may be due to the incorporation of dopant [21,22] to become grains very larger in Zn-doped porous SnO_2 bilayer films. After increasing the dopant percentage above 1% then predominant peaks of zinc occur in the XRD patterns, which collapses the structure of the element, hence, the lattice is elongated along with *a*-axis. It is evident from Table-1 that the grain size varies depending on the doping percentages, although they are all at the nanoscale level. Similarly, the results also demonstrated that the

TABLE-1
STRUCTURAL PARAMETERS OF POROUS Zn:SnO_2/SnO_2 THIN FILMS

Sample	Doping (%)	Lattice constant (Å)		Film thickness (μm)	Grain size (nm)	Dislocation density ($\times 10^{15}$) lines m^{-2}	Micro strain ($\times 10^{-3}$)
		a	c				
Porous Zn:SnO_2/SnO_2	0	4.6184	3.1393	213.22	33.72	0.879	32.22
	1	4.7783	3.1848	216.31	45.11	0.491	28.24
	2	4.8121	3.1848	219.32	49.02	0.416	22.11
	3	4.8946	3.1853	219.79	51.83	0.372	20.43

dislocation density and strain values for the various doping percentages are related to an increase in the quantity of defects, which is useful for the gas sensing characteristic [23,24].

FE-SEM studies: A field emission scanning electron microscope was used to examine the nanostructure of the synthesized porous thin films. Fig. 2 displays FESEM micrographs of the films that were deposited, magnified at a magnification of around 100K. The entire surface of the Zn:SnO_2/SnO_2 porous bilayer film is covered with flakes-like nano pores. Agglomerations with flat, spherical-shaped nanoparticles were observed in the porous films. As the particle size increases with increasing doping percentage these larger nanoparticles preferentially occupy the vacant spaces between the pores, resulting in a reduction in the amount of nano porosities. Hydrophilicity may be affected by a decrease in nano porosities [25,26].

EDAX studies: The quantitative analysis of the prepared thin film was carried out in order to determine the elemental composition of porous Zn:SnO_2/SnO_2 film. Fig. 3 shows the film composition which confirms the presence of Sn, O and Zn peaks in prepared corresponding samples. An average weight percentage of elements are shown in the inset of Fig. 3. The presence of silicon is due to the usage of glass substrate.

UV-visible studies: The relationship between photon energy and optical absorption for porous SnO_2 bilayer films with varying Zn doping percentages is depicted in Fig. 4a. The absorbance of the films was recorded at a wavelength above 200 nm. The maximum absorbance wavelength of the films was observed at 304 nm for 0% doping with zinc, 312 nm for 1% doping with zinc, 294 nm for 2% doping with zinc and 285 nm for 3% doping with zinc in porous SnO_2/SnO_2 thin film material. An optical band gap (E_g) has been estimated by using the data on the relationship between photon energy and absorbance. For direct allowed transitions, the optical absorption coefficient α at the absorption edge is provided by the following eqn. 1 [27]:

$$(\alpha h\nu)^2 = A\,(h\nu - E_g) \quad (1)$$

where A = absorption constant for a direct transition, h = Planck's constant, ν = photon frequency and E_g = optical band gap.

For direct allowed transition, band gap can be calculated by plotting $(\alpha h\nu)^2$ *vs*. $h\nu$ (Fig. 4b). The band gap energies of spray deposited films obtained at room temperature were found to be 3.5eV, 3.52eV for 0%, 1% Zn doped porous SnO_2/SnO_2 and 3.9 eV, 4.17 eV for 2, 3% of Zn doped SnO_2/SnO_2 thin films, respectively.

Photoluminescence (PL) studies: The influence of doping and porosity on the luminescence properties of the prepared

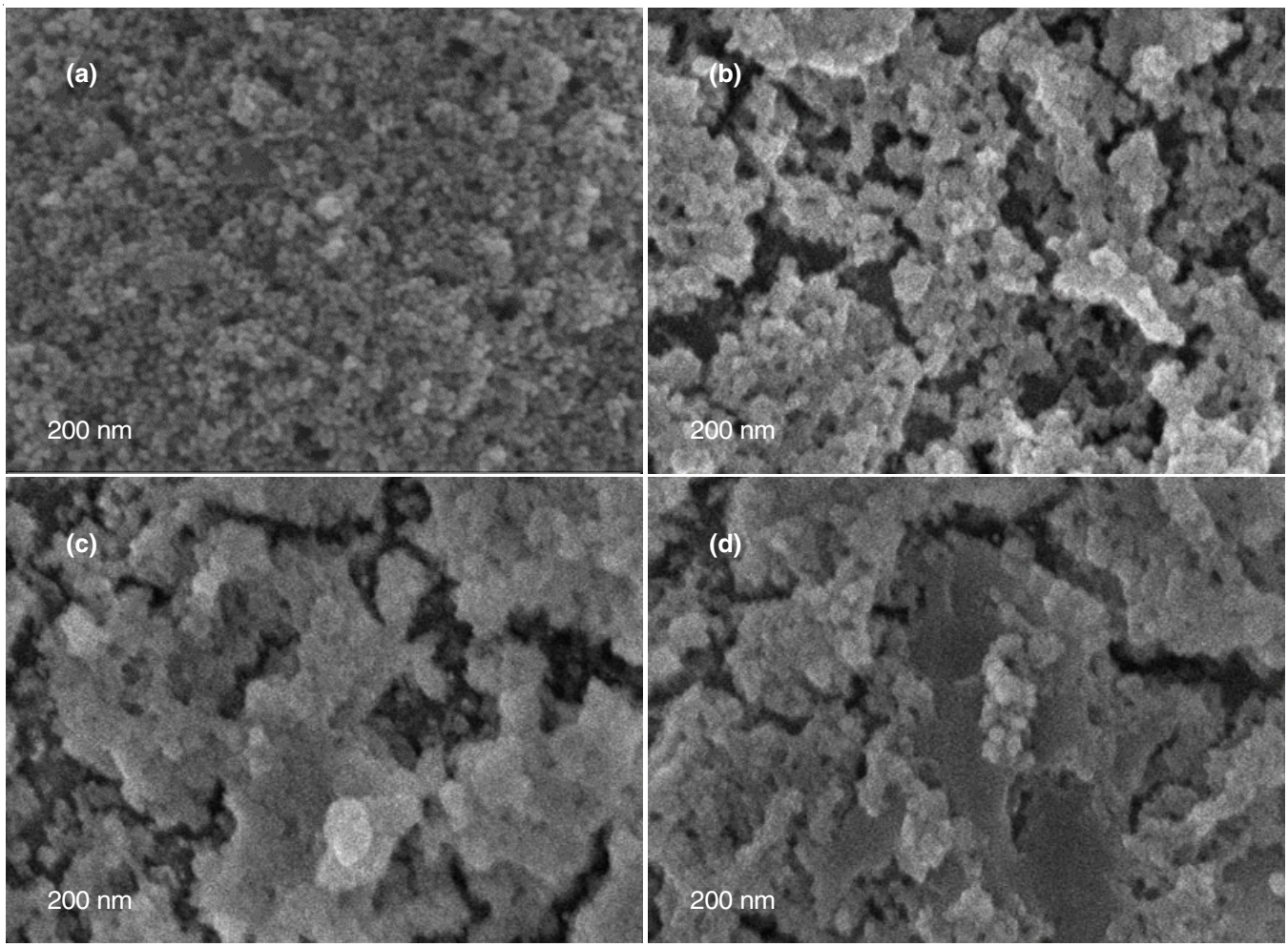

Fig. 2. Surface morphology of porous (a) 0% Zn, (b) 1% Zn, (c) 2% Zn, (d) 3% Zn:SnO_2/SnO_2 thin films

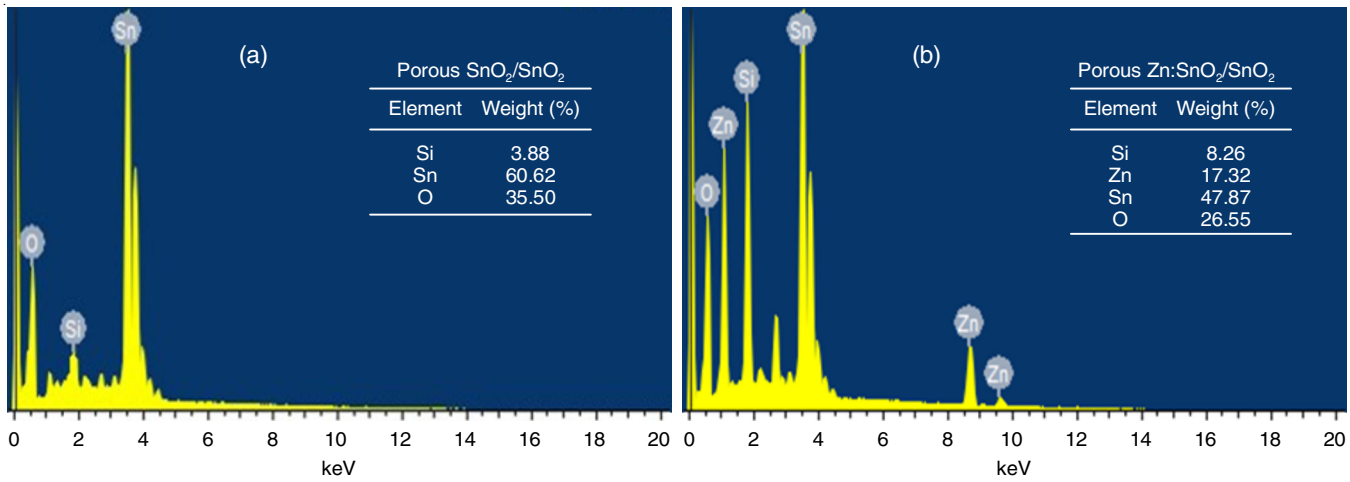

Fig. 3. Elemental composition of (a) porous SnO_2/SnO_2 and (b) porous Zn:SnO_2/SnO_2 bilayer thin film

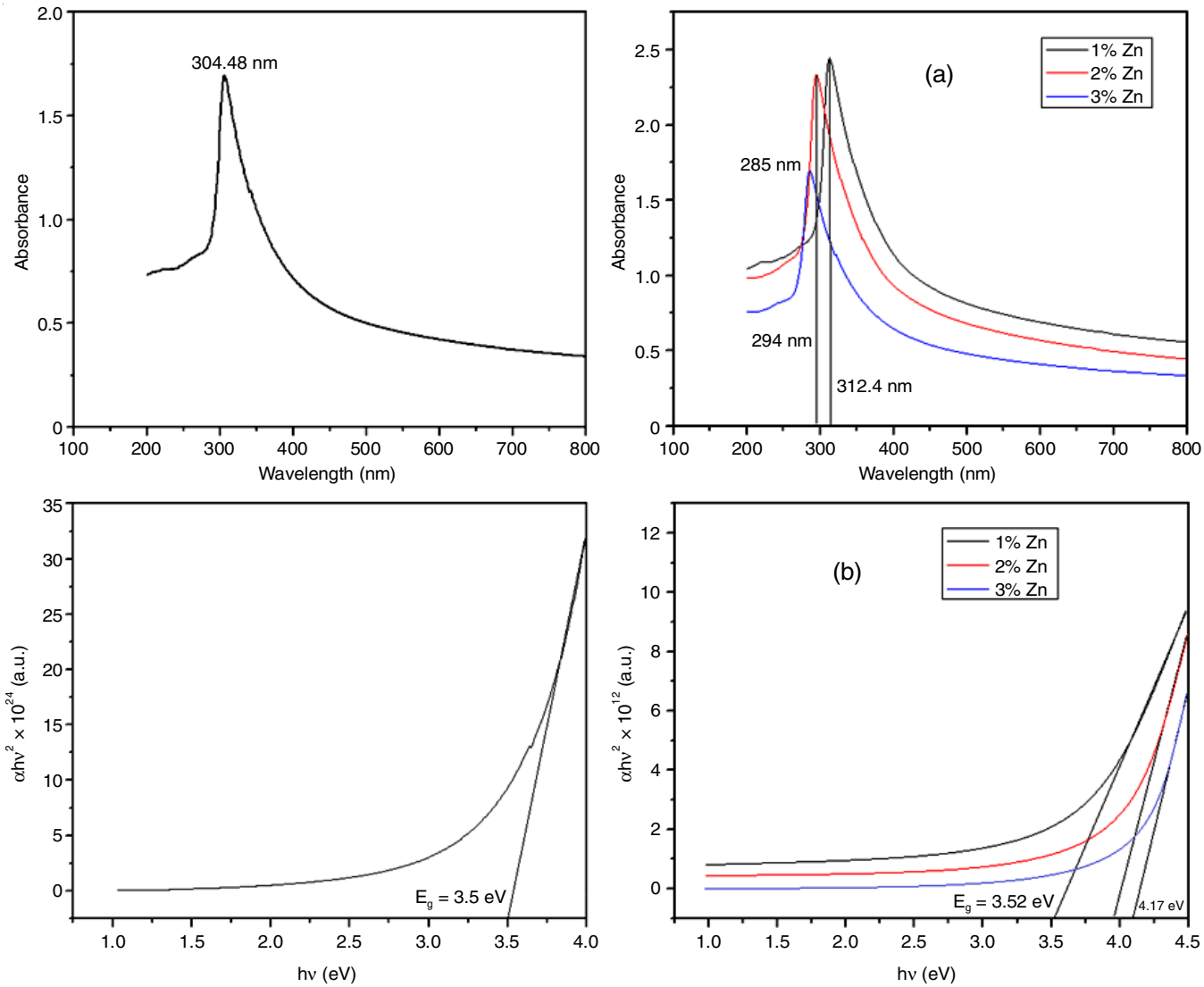

Fig. 4. UV-Vis absorbance spectra of (a) Zn:SnO_2/SnO_2 thin films (b) Plot of the $(\alpha h\nu)^2$ *vs.* photon energy (hν) for Zn:SnO_2/SnO_2 thin films

thin films was investigated using PL emission spectroscopy. The photoluminescence spectra of porous Zn-doped SnO_2/SnO_2 films containing various Zn doping percentages at room temperature are shown in Fig. 5a. The spectra of porous Zn-doped SnO_2/SnO_2 films exhibit a prominent emission peak at a wavelength above 275 nm. There is a significant difference seen in this PL spectra during increasing doping percentage. While introducing the dopant in porous SnO_2 bilayer film, the

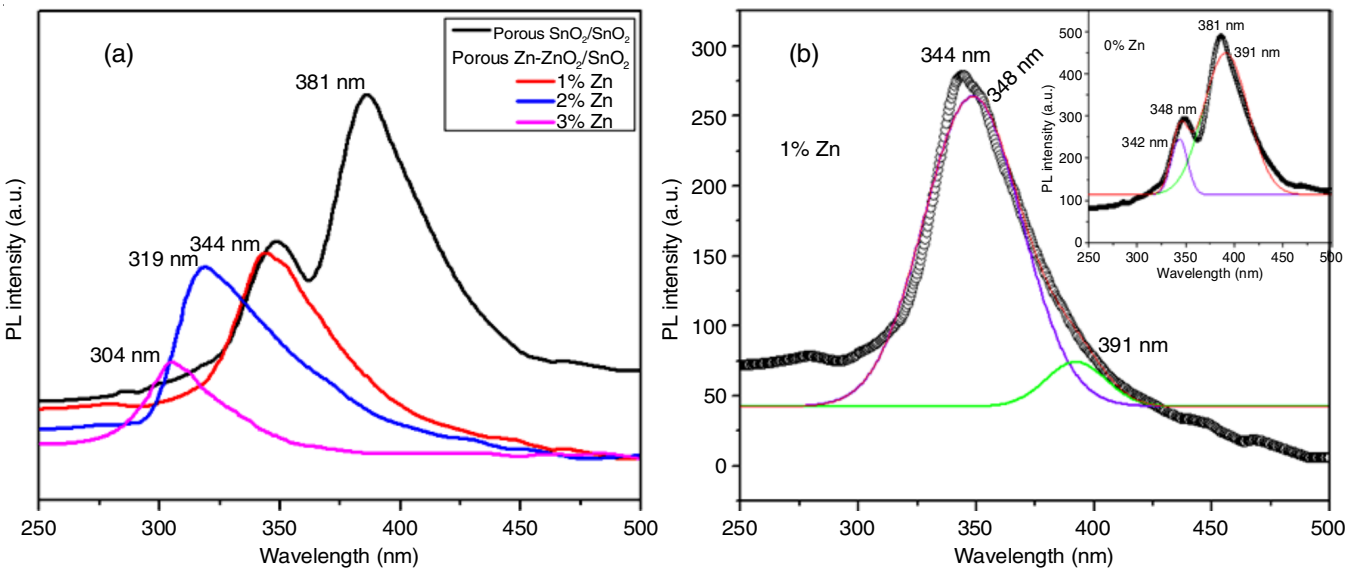

Fig. 5. PL spectra, deconvoluted PL of porous Zn:SnO_2/SnO_2 thin films

highest intensity peak in ~380 nm disappeared and another emission peak observed in 348 nm was decreased by increasing doping percentage. The PL intensity decreases due to the reduction in the distance between metal ions in the inter-band region as more metal is added and its concentration is increased. This phenomenon seems to be the result of concentration quenching [28,29]. The UV emission is produced by near band-edge emission from free-exciton recombination, whereas the visible emission is attributed to deep-level emission resulting from defects and impurities in the materials. The deconvoluted PL spectra of porous Zn doped SnO_2/SnO_2 thin films are shown in Fig. 5b. Deconvoluting and Gaussian fitting the peaks provide the individual contribution of the ultraviolet region in the PL spectra. It displays various wavelengths of UV emissions for different electron transitions within different types of defects.

The deep-level oxygen vacancies in the porous Zn-doped SnO_2 bilayer films are responsible for the near-ultraviolet emission peaks at wavelengths between 304 and 344 nm. A fully oxidized surface is less sensitive to gas detection than a surface deficient in oxygen. Defects, particularly oxygen vacancies, are commonly reported in determining the gas sensing characteristics of thin films [30]. Vacancies are well recognized for generating localized states around the fundamental band gap, either in the valence or conduction bands. A reduction in the density of oxygen deficiency with an increase in the dopant percentage is shown by a fall in the near-ultraviolet peak intensity.

Current-voltage characteristic (I-V): Fig. 6 displays the analyzed I-V characteristics of porous Zn-doped SnO_2 bilayer thin films at different dopant percentages. The I-V characteristics demonstrate almost linear rectification behaviour for all the prepared thin film samples. This demonstrates that the rectifying contact that occurs between a metal and a lightly doped semiconductor, a Schottky contact forms [31]. Depending on the doping percentage, the porous Zn-doped SnO_2 bilayer thin film has a resistance ranging from 500 kΩ to 670 kΩ. Because of the impact of the grain boundary, the electrical resistance of the spray-deposited thin film was highly dependent on the

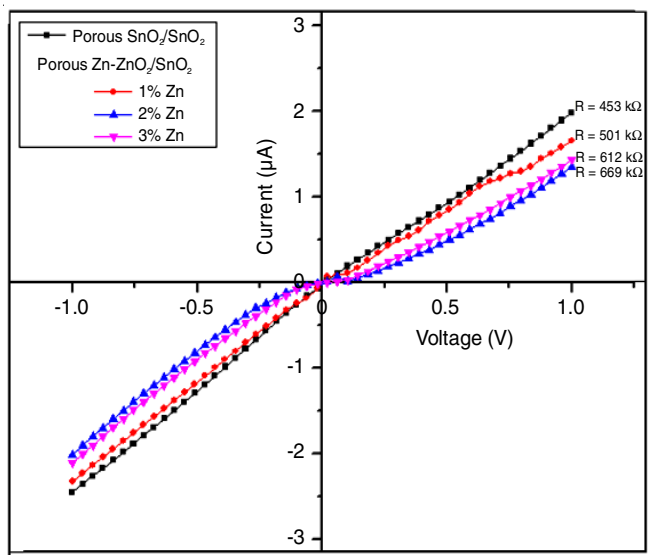

Fig. 6. I-V characteristics of porous Zn:SnO_2/SnO_2 thin films

dopant element and dopant percentage. When the dopant concentration exceeds above 1%, the grain boundary expands, resulting in a decrease in porosity diameter and reduced electrical resistance of the thin film. Grain boundaries and crystal lattice defects in the porous Zn doped SnO_2 bilayer thin film may have contributed to the decrease in electrical resistance seen in the film as the dopant percentage increased [32].

The resistance values for the prepared thin films deposited at different doping percentage were calculated by Ohm's law, which is as follows [33]:

$$V = IR$$

$$R = V/I \quad (2)$$

where V = voltage in volts, I= current in micro amps (μA); R = resistance in ohms. The calculated resistivity value is in the range of 453 kΩ, 501 kΩ, 669 kΩ and 612 kΩ for 0, 1, 2 and 3% of Zn doping SnO_2/SnO_2 films, respectively.

Gas sensing measurements: Studies on the gas response of porous Zn-doped SnO_2/SnO_2 thin films are carried out by using a dynamic gas response setup with different gases and different operating temperatures. The semiconducting gas sensors based on thin film metal oxide have been thoroughly investigated [34-37]. The gas response is determined by several parameters, including morphology, concentrations, film thickness and operating temperatures [38].

The gas response of porous Zn:SnO_2/SnO_2 films to several reducing and oxidizing gases, including NH_3, CO and NO_2, was investigated in the current work. The thin film sensor has been tested at temperatures ranging from room temperature to 200 ºC at a gas concentration of 50 ppm. A response bar chart of Zn:SnO_2/SnO_2 film interacting with various gases at different operating temperatures is displayed in Fig. 7. It was observed that the maximum response values are achieved by 1% of Zn-doped porous SnO_2/SnO_2 film (1.07018) towards CO at 200 ºC.

The dynamic response of porous Zn:SnO_2/SnO_2 film estimated for CO gas at concentrations between 50 and 400 ppm at 200 ºC is shown in Fig. 8a. The response is determined as the ratio between the resistance value of the film in air (R_a) and the film in the tested gas (R_g). However, for porous Zn:SnO_2/SnO_2 thin films with increasing gas concentrations shows a significant response towards CO gas is observed. The relationship that was fitted to the various CO gas concentration ranges is depicted in Fig. 8b. This fitted curve revealed an almost linear relationship between the response and gas concentration. Based on the experimental data, y = 0.000187x + 1.06758 is the linearity and $R^2 = 0.97312$ is the relative correlation coefficient. This provides the possibility of accurately measuring the concentration of CO gas.

Limit of detection: The lowest detection limit (LDL) were determined by using this linear fit data and determined to be 0.015 ppm. The following relationship was used to calculated lowest detection limit [39]:

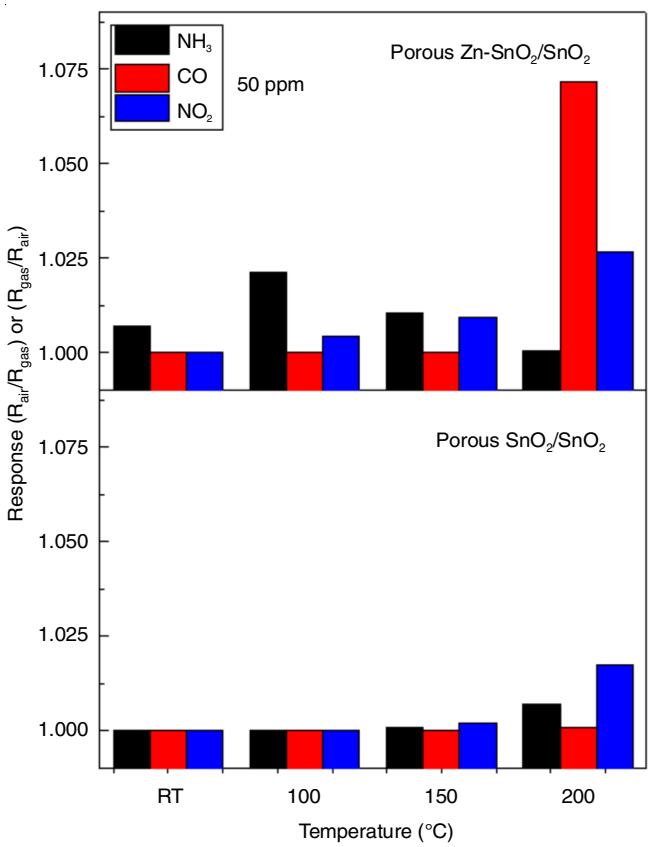

Fig. 7. Different gas response at different temperature of porous Zn doped SnO_2/SnO_2 thin films

$$LDL = \frac{3.3 \times \text{Standard deviation in intercept}}{\text{Slope}} \quad (3)$$

The standard deviation in intercept is:

$$b = a\sqrt{n} \quad (4)$$

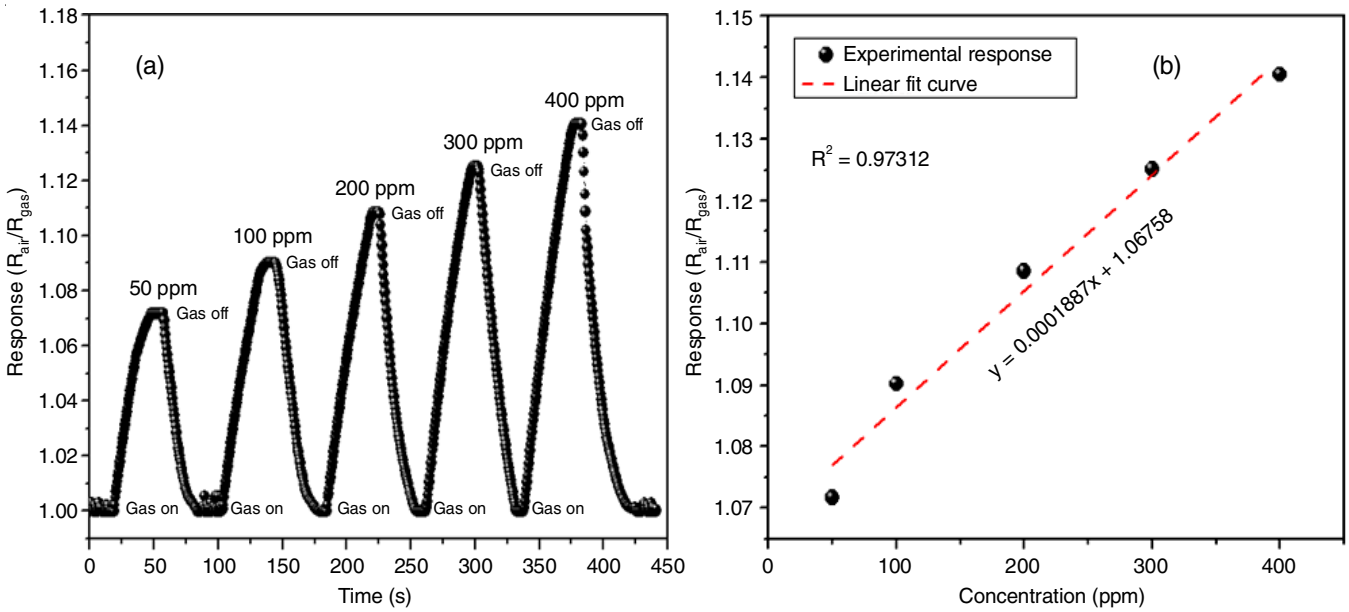

Fig. 8. (a) Dynamic response of CO gas with different gas concentration of porous Zn:SnO_2/SnO_2 thin film at 200 °C, (b) Linear fit of gas response *versus* concentration

where a is the standard error of the intercept and n is the total number of calculated points.

Response and recovery time: At 200 ºC, the response and recovery of porous Zn:SnO_2/SnO_2 thin film towards 50 ppm CO gas were measured and the results are shown in Fig. 9. In absence of gas, the baseline seems to be remain nearly constant. The porous Zn:SnO_2/SnO_2 sensor exhibits quick response/recovery time and a high response value to CO gas due to the porous structure and significant specific surface area of the film as well as the quantity of chemisorbed oxygen ions on its surface. The results showed that the response and recovery times were, respectively 27 and 27 s. While selecting a gas sensor for practical applications, it is essential to consider its long-term functional stability.

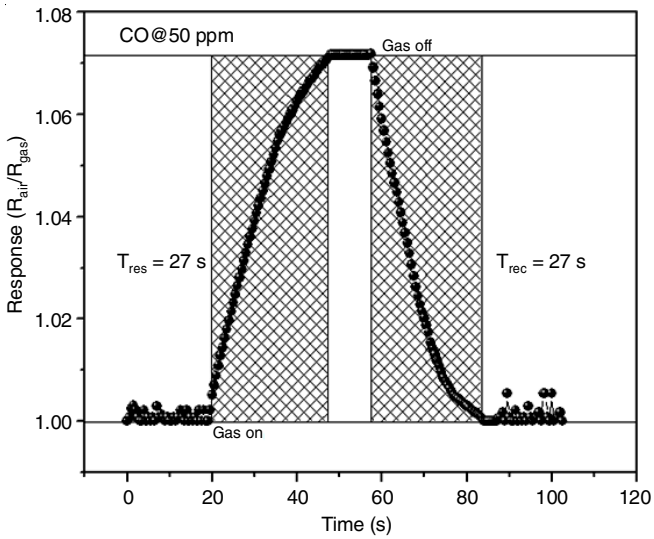

Fig. 9. Response and recovery time of porous Zn:SnO_2/SnO_2 thin film at 50 ppm of CO gas at 200 °C

Long term and short term stability: The change in the R_{air}/R_{gas} ratio of 1% of Zn-doped porous SnO_2 bilayer film is shown in Fig. 10a during it is exposure to 400 ppm of CO gas for five continuous cycles of gas on and off at 200 ºC. As can be observed, there is almost zero variation, indicating excellent repeatability and extremely strong short-term stability.

Furthermore, 1% of Zn-doped porous SnO_2 bilayer sensor was exposed to a flow rate of 50 ppm and 400 ppm of CO gas for eight weeks at 200 °C, as shown in Fig. 10b. This exposure was repeated once a day in the first week and once a week for up to 8 weeks. The results indicated that the first response of the sensor remained essentially the same throughout 56 days of continuous testing, which showed that the material used to manufacture the sensor was of good quality and having long-term use. Throughout the procedure, the response value of the sensor remained around 99.92%, which indicated the great capacity for reuse and durability of the sensor.

Conclusion

The porous zinc doped tin oxide thin films were fabricated successfully by automated nebulizer spray pyrolysis (ANSP) technique. The XRD, EDAX, FESEM, UV-visible, photoluminescence spectroscopy, IV characteristic and gas sensor performance were used to analyze the prepared thin films. The XRD patterns revealed the structural properties of prepared samples, the calculated grain size seems to be increased with increasing dopant percentage. The FESEM micrographs depicted the surface morphology of the prepared thin films and the presence of respective elements were confirmed by EDAX. The optical properties were examined by UV-visible and photoluminescence. The IV characteristic graph shows the super linear resistance behaviour. The gas detecting behavior of the films was investigated using a dynamic approach, which demonstrates that 1% of Zn doped porous SnO2/SnO2 thin film sensor is sensitive and selective towards CO gas, with a short reaction and recovery time. Thus, it can be assumed that the prepared Zn doped porous SnO_2/SnO_2 thin film fabricated with 1% of Zn doping has the potential to be an effective CO gas sensor.

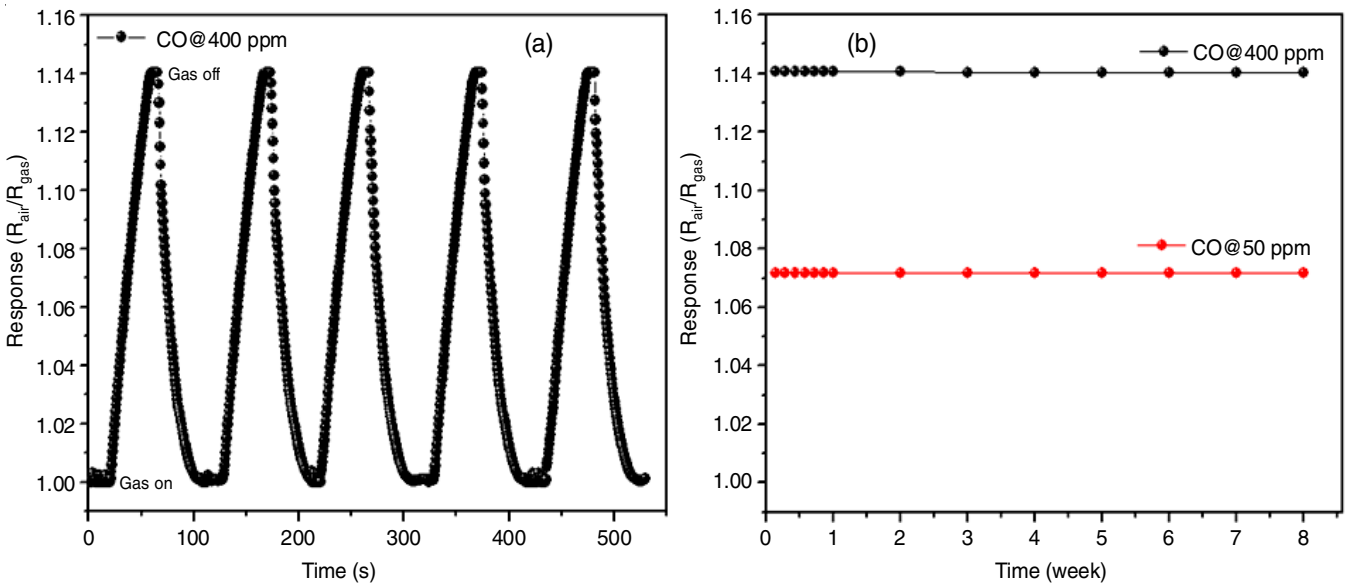

Fig. 10. (a) Short-term stability and (b) Long-term stability of porous Zn-SnO_2/SnO_2 thin film at 200 °C

CONFLICT OF INTEREST

The authors declare that there is no conflict of interests regarding the publication of this article.

REFERENCES

1. S. Dhall, B.R. Mehta, A.K. Tyagi and K. Sood, *Sensors Int.*, **2**, 100116 (2021); https://doi.org/10.1016/j.sintl.2021.100116
2. Z. Yuan, R. Li, F. Meng, J. Zhang, K. Zuo and E. Han, *Sensors*, **19**, 1495 (2019); https://doi.org/10.3390/s19071495
3. R. Xavier, L. Thirumalaisamy, S. Madhanagurusamy and K. Sivaperuman, *Ceram. Int.*, **50**, 969 (2024); https://doi.org/10.1016/j.ceramint.2023.10.187
4. R. Godiwal, A.K. Gangwar and P. Singh, *Mater. Lett.*, **357**, 135787 (2024); https://doi.org/10.1016/j.matlet.2023.135787
5. M.H. Mahmood and M.A. Maleque, *Arab. J. Sci. Eng.*, **46**, 6557 (2021); https://doi.org/10.1007/s13369-020-05233-8
6. M. Koèí, T. Izsák, G. Vanko, M. Sojková, J. Hrdá, O. Szabó, M. Husák, K. Végsö, M. Varga and A. Kromka, *ACS Appl. Mater. Interfaces*, **15**, 34206 (2023); https://doi.org/10.1021/acsami.3c04438
7. L. Liu, Y. Wang, Y. Liu, S. Wang, T. Li, S. Feng, S. Qin and T. Zhang, *Microsyst. Nanoeng.*, **8**, 85 (2022); https://doi.org/10.1038/s41378-022-00410-1
8. X. Lu, S. Zhang, J. Xing, Y. Wang, W. Chen, D. Ding, Y. Wu, S. Wang, L. Duan and J. Hao, *Engineering*, **6**, 1423 (2020); https://doi.org/10.1016/j.eng.2020.03.014
9. C. Yan, H. Li and Z. Li, *Front. Public Health*, **10**, 930780 (2022); https://doi.org/10.3389/fpubh.2022.930780
10. I. Manisalidis, E. Stavropoulou, A. Stavropoulos and E. Bezirtzoglou, *Front. Public Health*, **8**, 14 (2020); https://doi.org/10.3389/fpubh.2020.00014
11. P. Zhou, Y. Shen, S. Zhao, G. Li, Y. Yin, R. Lu, S. Gao, C. Han and D. Wei, *J. Alloys Compd.*, **789**, 129 (2019); https://doi.org/10.1016/j.jallcom.2019.03.038
12. D. Xu, Q. Yu, T. Chen, S. Zhong, J. Ma, L. Bao, L. Zhang, F. Zhao and S. Du, *Materials*, **11**, 1840 (2018); https://doi.org/10.3390/ma11101840
13. J.M. Calderon-Moreno, S. Preda, L. Predoana, M. Zaharescu, M. Anastasescu, M. Nicolescu, M. Stoica, H. Stroescu, M. Gartner, O. Buiu, M. Mihaila and B. Serban, *Ceram. Int.*, **40**, 2209 (2014); https://doi.org/10.1016/j.ceramint.2013.07.139
14. W. Huang, M. Lei, H. Huang, J. Chen and H. Chen, *Surf. Coat. Technol.*, **204**, 3954 (2010); https://doi.org/10.1016/j.surfcoat.2010.03.030
15. R.D. Prabu, S. Valanarasu, V. Ganesh, M. Shkir, A. Kathalingam, S. AlFaify, S.R. Srikumar and R. Chandramohan, *Mater. Sci. Semicond. Process.*, **74**, 129 (2018); https://doi.org/10.1016/j.mssp.2017.10.023
16. V.G. Krishnan and P. Elango, *Surf. Rev. Lett.*, **28**, 2050029 (2021); https://doi.org/10.1142/S0218625X20500298
17. V.G. Krishnan, P. Elango, M. Ragavendar, P. Sathish and G. Gowrisankar, *Mater. Res. Express*, **4**, 036401 (2017); https://doi.org/10.1088/2053-1591/aa6077
18. L. Soussi, T. Garmim, O. Karzazi, A. Rmili, A. El Bachiri, A. Louardi and H. Erguig, *Surf. Interfaces*, **19**, 100467 (2020); https://doi.org/10.1016/j.surfin.2020.100467
19. L. Zhang, W. Xu, W. Liu, P. Cao, S. Han, D. Zhu and Y. Lu, *J. Phys. D Appl. Phys.*, **53**, 175106 (2020); https://doi.org/10.1088/1361-6463/ab6ea0
20. M. Ayadi, O. Benhaoua, M. Sebais, O. Halimi, B. Boudine and M.S. Aida, *Mater. Res. Express*, **6**, 076407 (2019); https://doi.org/10.1088/2053-1591/ab10c5
21. S. Senthilkumaar, K. Rajendran, S. Banerjee, T.K. Chini and V. Sengodan, *Mater. Sci. Semicond. Process.*, **11**, 6 (2008); https://doi.org/10.1016/j.mssp.2008.04.005
22. S.S. Shinde, A.P. Korade, C.H. Bhosale and K.Y. Rajpure, *J. Alloys Compd.*, **551**, 688 (2013); https://doi.org/10.1016/j.jallcom.2012.11.057
23. F. Ricciardella, S. Vollebregt, R. Tilmann, O. Hartwig, C. Bartlam, P.M. Sarro, H. Sachdev and G.S. Duesberg, *Carbon Trends*, **3**, 100024 (2021); https://doi.org/10.1016/j.cartre.2021.100024
24. P.G. Choi, T. Fuchigami, K. Kakimoto and Y. Masuda, *ACS Sens.*, **5**, 1665 (2020); https://doi.org/10.1021/acssensors.0c00290
25. F. Ghorban and A. Eshaghi, *Opt. Quantum Electron.*, **49**, 67 (2017); https://doi.org/10.1007/s11082-017-0904-z
26. S. Wang, K. Zou, Y. Qian, Y. Deng, L. Zhang and G. Chen, *Carbon*, **144**, 745 (2019); https://doi.org/10.1016/j.carbon.2018.12.113
27. V.S. Vinila and J. Isac, in eds.: S. Thomas, N. Kalarikkal and A.R. Abraham, Synthesis and Structural Studies of Superconducting Perovskite $GdBa_2Ca_3Cu_4O_{10.5+ä}$ Nanosystems, In: Micro and Nano Technologies, Design, Fabrication and Characterization of Multifunctional Nanomaterials, Elsevier, Chap. 14, pp. 319-341 (2022).
28. P.A. Hind, P.S. Patil, N.B. Gummagol, U.K. Goutam and B.V. Rajendra, *J. Mater. Res.*, **38**, 4828 (2023); https://doi.org/10.1557/s43578-023-01020-x
29. J.-S. Park, D. Kim, W.-B. Kim and I.-K. Park, *Ceram. Int.*, **46**, 430 (2020); https://doi.org/10.1016/j.ceramint.2019.08.279
30. X. Wang, P. Ren, T. Hailin, H. Fan, C. Cai and W. Liu, *J. Alloys Compds*, **669**, 29 (2016); https://doi.org/10.1016/j.jallcom.2016.01.225
31. G.G. Pethuraja, R.E. Welser, A.K. Sood, C. Lee, N.J. Alexander, P. Haldar, H. Efstathiadis, and J.L. Harvey, *Adv. Mater. Phys. Chem.*, **2**, 59 (2013); https://doi.org/10.4236/ampc.2012.22010
32. I. Bibi, S. Iqbal, F. Majid, S. Kamal, Q. Raza, M. Amami, K.M. Katubi, N. Alwadai, M. Asad Kareem and M. Iqbal, *Results Phys.*, **40**, 105868 (2022); https://doi.org/10.1016/j.rinp.2022.105868
33. B. Carter, Review of Op Amp Basics, In: Op Amps for Everyone, Newnes, eds. 4, Chap. 2, pp. 7-17 (2013).
34. G.F. Fine, L.M. Cavanagh, A. Afonja and R. Binions, *Sensors*, **10**, 5469 (2010); https://doi.org/10.3390/s100605469
35. A. Afzal, *J. Materiom.*, **5**, 542 (2019); https://doi.org/10.1016/j.jmat.2019.08.003
36. K. Sivaperuman, A. Thomas, R. Thangavel, L. Thirumalaisamy, S. Palanivel, S. Pitchaimuthu, N. Ahsan and Y. Okada, *Prog. Mater. Sci.*, **142**, 101222 (2024); https://doi.org/10.1016/j.pmatsci.2023.101222
37. S.L. Bhise, L.H. Kathwate, G. Umadevi, K.G. Krishna, V.D. Mote and B.N. Dole, *J. Mater. Sci. Mater. Electron.*, **35**, 66 (2024); https://doi.org/10.1007/s10854-023-11780-1
38. S.S. Badadhe and I.S. Mulla, *Sens. Actuators B Chem.*, **156**, 943 (2011); https://doi.org/10.1016/j.snb.2011.03.010
39. A. Sanger, S.B. Kang, M.H. Jeong, C.U. Kim, J.M. Baik and K.J. Choi, *ACS Appl. Electron. Mater.*, **1**, 1261 (2019); https://doi.org/10.1021/acsaelm.9b00210